MIT Open Access Articles

Mechanical and Structural Characterization of Semicrystalline Polyethylene under Tensile Deformation by Molecular Dynamics Simulations

Mechanical and Structural Characterization of Semicrystalline Polyethylene under Tensile Deformation by Molecular Dynamics Simulations

In-Chul Yeh[1], Jan W. Andzelm[1,], and Gregory C. Rutledge[2,*]*

[1]Macromolecular Science & Technology Branch, Materials & Manufacturing Science Division, U.S. Army Research Laboratory, Aberdeen Proving Ground, Maryland 21005, USA

[2]Department of Chemical Engineering, Massachusetts Institute of Technology, 77 Massachusetts Avenue, Cambridge, Massachusetts 02139, USA

ABSTRACT. We have studied tensile deformations of semicrystalline polyethylene (PE) with molecular dynamics simulations at two different strain rates and temperatures. Compared to earlier studies, the modeled systems were approximately five times larger, which allowed significantly larger strains up to about 120% to be examined. Two different modes of structural transformation of semicrystalline PE were observed at the higher temperature of 350 K, depending on the strain rate. At the faster strain rate of 5×10^7 s^{-1}, cavitation in the non-crystalline region dominated, with little change in the crystalline region, resulting in monotonically declining stress with increasing strain after the yield point. However, in a small number of cases,

significant deviations from the average stress-strain profile were observed that correlated with topological constraints, such as bridges and bridging entanglements connecting crystalline regions separated by the non-crystalline region, and destabilization of the crystalline region. At the slower strain rate of 5×10^6 s^{-1}, we observed repeated melting/recrystallization events and significant oscillations in stress associated with variations of density in crystalline and non-crystalline regions and the displacement of polymer chains from crystalline to non-crystalline regions. When averaged over an ensemble of starting configurations for semicrystalline PE, the oscillations were found to be less coherent from microstate to microstate and offset one another. The post-yield stress became notably smoother, and began to resemble the plastic flow observed macroscopically, followed by stress hardening at the later stage of deformation. At the lower temperature of 250 K, cavity formation was the only mechanism observed, for both strain rates. The interplay between the thermodynamic stability of the crystalline region and the topological constraints imposed by bridges and entanglements in the non-crystalline region is crucial to understanding structural transformations of semicrystalline PE during tensile deformations.

Introduction

Semicrystalline polyethylene (PE) possesses unique thermal and mechanical properties and is widely used in many consumer and industrial materials. Its thermal and mechanical properties depend sensitively on the fraction of crystalline content as well as processing conditions. The interplay between crystalline and non-crystalline domains can affect the observed thermal and mechanical properties of semicrystalline polymers. There have been significant experimental efforts to characterize and improve thermal and mechanical properties of semicrystalline PE.[1-3] Molecular dynamics (MD) simulation is a useful technique to study

polymeric systems in atomistic detail and uncover underlying structural mechanisms for the observed thermal and mechanical properties to complement the experimental efforts. Although several different theoretical and computational models for semicrystalline polymers have been proposed,[4-8] MD simulations of semicrystalline polymers, where crystalline and amorphous domains coexist, are significantly more challenging compared to simulations of pure crystalline or amorphous phases. Nevertheless, Rutledge and coworkers have developed an Interphase Monte Carlo (IMC) method to prepare models of semicrystalline PE suitable for MD simulations[9,10] and conducted extensive simulation studies investigating the mechanical response of semicrystalline PE.[11] Recently, Kim et al.[12] studied deformations of semicrystalline PE using MD simulations under constant lateral stress conditions. Two distinct mechanisms for structural transformations in semicrystalline PE, cavity formation and melting/recrystallization, were observed during tensile deformations at two different strain rates. However, the lateral dimensions of the systems used in that study were rather small, and tensile deformation was limited up to 49% strain. Full effects of topological features such as entanglements on mechanical properties and the details of structural transformations during deformations can be investigated better with a bigger system size and larger strains.[1,13] In this study, we replicate the earlier study of Kim et al.[12] using systems that are approximately five times larger than theirs, and an ensemble that comprises an order of magnitude larger number of configurations. We performed tensile deformation simulations at constant lateral stress for strains as large as 120% to capture the structural and dynamical details of semicrystalline PE during tensile deformations at these larger strains. We investigated the effects of topological features, entanglements, strain rates, and temperature on the mechanical properties of semicrystalline PE.

Methods

Interphase Monte Carlo equilibration

We used the IMC methodology of Rutledge and co-workers[9-11] as implemented in the EMC (Enhanced Monte Carlo)[14,15] version 9.3.6 software with a united-atom (UA) force field[10,16] to generate 100 starting configurations of semicrystalline PE. The typical simulation set-up is illustrated in Figure 1 (a). Initially, a unit cell of the crystalline PE containing two chains of two methylene groups each was replicated 6 and 10 times in the two lateral directions and 120 times in the lamellar stack or z direction. The resulting lengths of the simulation cell in x, y, and z directions were 5.535, 4.445, and 25.366 nm, respectively; these dimensions were fixed during IMC equilibrations. Compared to the system size used by Kim et al.,[12] each lateral dimension was doubled, while the z dimension was increased 1.2 times. The crystalline chain stems were tilted so that the {201} crystallographic plane was normal to the z direction. Half of the simulation cell remained crystalline while the other half was transformed to a non-crystalline region 12.7 nm thick. Twenty-four bonds were cut in the non-crystalline region, resulting in 48 end-sites in each configuration, and 2136 UA sites were removed in the non-crystalline region to match the density of amorphous PE, which has been estimated to be 0.855 g/cm^3 at 298 K.[17] The resulting semicrystalline configuration contained 26664 UA sites. Then the non-crystalline region was subjected to equilibration by IMC with a set of Monte Carlo (MC) moves that includes both local rearrangements and alterations of chain topology. Further details of the MC moves and the preparation method with the IMC methodology can be found in earlier studies with smaller systems.[11,12] The same MC move set described by Lee and Rutledge[11] was used. We also compared topological features of the configurations prepared with different relative frequencies of MC moves, and no significant differences were observed after sufficiently long MC equilibrations. The IMC equilibration started with 10000 MC cycles at 10000 K followed by

cooling to 350 K during 10000 cycles. Then, six successive sessions of simulation by IMC at 350 K were performed with 40000 MC cycles at each session. Semicrystalline PE configurations prepared in this manner consist of chains with polydisperse molecular weight distributions containing loop, tail, and bridge segments as illustrated in Figure 2 (a). Each polymer chain was unwrapped from the wrapped configuration in the primary simulation cell, and the topological features of each chain were determined. Loops connect crystal stems on the same side of the non-crystalline region. Bridges connect crystal stems that are separated by the non-crystalline region. Tails are segments of chains connected at only one end to a crystal stem. These topological features were analyzed after each session of IMC simulation to check the progress of equilibration. As noted previously,[12] cyclic chains (or cycles) containing 2 or more crystal stems can be formed as illustrated in Figure 2 (a). However, topological features (e.g. loops) within cyclic chains have not been analyzed in this work, and all the reported topological features were obtained by analyzing only the linear chains, with two end sites apiece. The average number of UA sites in the linear chain was 1078 with a standard deviation of 782. The polydispersity index, defined as the ratio of the mass average molecular weight to the number average molecular weight, was 1.53. Figure 2 (b) shows the change during IMC equilibration of the topological features illustrated in Figure 2 (a). The rate of change in topological features decreased significantly near the end of the IMC equilibration. The number of bridge segments increased with the progress of equilibration. At the end of the IMC equilibration, an average of 1.29 bridge segments were identified for each configuration, and 66 out of 100 configurations had one or more bridge segments. The number of atoms in each bridge segment decreased gradually with continued simulation, ending up with an average bridge length of 565 UA sites after the last stage of IMC equilibration. The number of loop segments and the average length of a loop

segment increased gradually during the IMC equilibration, ending up with 86.28 loops in each

configuration, with an average loop length of 38.65 UA sites. The total number of tail segments

was fixed at 4800 (i.e. 48 tail segments in each of 100 configurations), but the average tail

segment length was observed to decrease as the IMC equilibration progressed. The average

number of cyclic chains in each configuration also decreased to 2.52 after the last stage of

equilibration. Figure 2 (b) shows the full length distributions of bridge, loop, and tail segments at

the end of the IMC equilibration. Even though the lengths of loops and tails were dominated by

short segments, longer loops and tails were present, as expected according to topological

equilibration.[18] These segments are expected to play an important role in the mechanical

properties of semicrystalline PE through their entanglements.

Energy minimization and molecular dynamics equilibration

The semicrystalline PE was modeled by a united-atom (UA) force field originally

developed by Paul et al.[16] to reproduce properties of melts of *n*-alkane chains of varying

molecular weights and slightly modified by Chang et al.[19] The same UA force field was used in

recent simulations of semicrystalline PE.[11,12] The LAMMPS package[20] was used to perform all

energy minimizations and MD simulations. Unless specified otherwise, the temperature was

maintained at 350 K with a Nosé-Hoover thermostat[21] with a temperature damping constant of 10

fs, and a time step of 2 fs was used. The temperature of 350 K, which lies between glass

transition and melting temperatures of PE,[22] was chosen to observe diverse deformation

behaviors of semicrystalline PE, and so that our results could be compared with those from

previous simulations[11,12] with smaller system sizes performed at the same temperature. One

hundred configurations prepared by equilibration using IMC were equilibrated further with brief

energy minimizations followed by 8-ns MD simulations under constant stress conditions using a

Nosé-Hoover barostat[21] with a target stress of 0.1 MPa and a stress damping parameter of 1 ps applied independently in the three orthogonal directions. In about 15% of the cases, it was found useful to precede the constant pressure MD simulations with a short, 10-ps constant volume simulation using a smaller time step of 1 fs to relax the initial configurations properly. The non-bonded interactions within the cutoff distance $r_c = 2.5\sigma$ (1.00225 nm), where σ is the UA van der Waals diameter, were calculated explicitly with a Lennard-Jones potential. The non-bonded interactions beyond r_c were taken into account with a long-range van der Waals tail correction to the energy and pressure.[23] Simulations of tensile deformation along the z direction up to the strain of 1.23 were performed at 350 K, with two different strain rates of 5×10^7 s^{-1} and 5×10^6 s^{-1}, starting from the last equilibrated configuration for each of the 100 systems. The lateral components of stress were maintained independently at 0.1 MPa during tensile deformations. We also performed simulations of tensile deformation at 250 K and the strain rates of 5×10^7 s^{-1} and 5×10^6 s^{-1} after 8-ns further equilibrations under constant stress conditions at the same temperature, to examine the effects of the temperature on the deformation mechanisms.

To compare to the earlier results of Kim et al.[12] and to evaluate the effects of system size and crystallinity, we also performed tensile deformation simulations of semicrystalline PE using the smaller system size of Kim et al.[12] with 100 equilibrated configurations as well as deformation simulations of purely amorphous and crystalline PE samples at the strain rate of 5×10^7 s^{-1} for strains up to 0.49. The starting configurations of amorphous PE were prepared by performing 8-ns constant pressure simulations, starting from eight different semicrystalline PE configurations, at an elevated temperature of 700 K. During these simulations, the initial semicrystalline configurations were observed to melt, and the systems were changed to the amorphous configurations. These elevated temperature simulations were followed by contant

pressure simulations at the lower temperature of 350 K for an additional 8 ns. Even though amorphous PE systems prepared in this manner contain chains with polydisperse molecular weight distributions, no significant differences in estimated densities were observed among the runs with eight different starting configurations. The purely crystalline PE was prepared and subjected to an 8-ns constant pressure MD simulation at 350 K. The data from the last 4 ns of each simulation were used to estimate mass densities of PE in purely amorphous and crystalline phases. During the tensile deformation of crystalline PE, non-diagonal components of the stress tensor (xy, yz, and xz) were maintained at zero to allow the maximum flexibility of the simulation cell and to minimize the shear stress due to the fixed tilt factors.

Order parameter

Each UA site i was classified as either crystalline or non-crystalline according to its local order parameter $P_{2,i} = (3<\cos^2\theta_{ij}> - 1)/2$, averaged over all UA sites j within the van der Waals cutoff distance r_c of 1.00225 nm, where θ_{ij} is the angle between the vector from site $i - 1$ to $i + 1$ and that from $j - 1$ to $j + 1$. All sites having $P_{2,i} > 0.4$ were designated as crystalline, as recommended by Yi et al.[24]

Entanglement analysis

Most theoretical and computational models of polymer entanglements were developed with isotropic amorphous polymers in mind. However, semicrystalline polymers contain both crystalline and non-crystalline regions with different degrees of entanglement. Care has to be taken to study entanglements in such an inhomogeneous system.[25,26] Methods based on purely geometric criteria, such as the Z-code[27] used in this work, are preferred for the analysis of entanglements in semicrystalline polymers. First, we analyzed the entanglement statistics of the

non-crystalline region, and we focused on tensile deformations at the faster strain rate of 5×10^7 s^{-1} because of the complexity in defining crystalline and non-crystalline segments after multiple melting/recrystallization events at the slower strain rate of 5×10^6 s^{-1}, as described later. Two different estimators of entanglement length N_e (the number of monomers between entanglements) were used to analyze entanglement statistics in the non-crystalline region. The first estimator of N_e (which we denote as $N_{e,\text{coil}}$) is given by the following relation[27-29]

$$N_{e,\text{coil}}(N) = (N-1)\frac{R_{ee}^2}{L_{pp}^2} , \tag{1}$$

where N is the chain length (the total number of monomers in the chain), R_{ee}^2 is the squared end-to-end distance of the chain, and L_{pp} is the contour length of the primitive path determined by the Z-code. The other estimator of N_e (which we denote as $N_{e,\text{kink}}$)[29] is

$$N_{e,\text{kink}}(N) = \frac{N(N-1)}{Z_{nc}(N-1)+N} , \tag{2}$$

where Z_{nc} is the number of kinks (entanglement points) in each chain segment in the non-crystalline region determined by the Z-code. The non-crystalline region included the highly oriented chain segments spanning the cavity region between the crystalline lamellae at the later stages of tensile deformations, even though the nominal order parameter $P_{2,i}$ values of UA sites belonging to these chain segments might have been higher than 0.4. Input coordinates for the non-crystalline region for the Z-code were prepared by replicating the simulation cell to form nearest neighbor images in both lateral directions (for a total of 9 cells) to avoid the finite-size problems described by Foteinopoulou et al.[30] All the unique pairs of chain segments forming entanglements were identified using the Z-code. Then, among the entanglement pairs, bridging entanglements[12] that form between tails or loops belonging to opposing crystalline regions were

singled out and analyzed. Such entanglements can play an important role during tensile

deformations. To investigate the effects of topological features during deformations, we analyzed

entanglement statistics at several stages during tensile deformations.

We also analyzed entanglement statistics within the entire simulation cell containing both

crystalline and non-crystalline regions by monitoring the overall average number of

entanglements $\langle \bar{Z}_{sc} \rangle$, where Z_{sc} is the number of entanglements in each full-length

semicrystalline PE chain containing both crystalline and non-crystalline regions calculated by the

Z-code, and overbar and angle bracket signify averages over chains in each configuration and

over the ensemble of configurations, respectively. Input coordinates for the Z-code were

prepared by replicating the simulation cell three times in each of three directions (27 times

overall) to minimize the finite-size problems.

Results and Discussions

Z-direction density profiles

We calculated mass-density profiles along the *z*-direction of the simulation cell for

configurations taken from the last 4 ns of equilibration with constant-pressure MD simulations

using a bin width of 0.1 nm. The calculated *z*-direction density profile in Figure 1 (b) shows

well-defined crystalline, interphase, and amorphous regions across the *z* direction. The average

dimensions of the simulation cell in *x*, *y*, and *z* directions were 5.54 ($\pm$ 0.10), 4.73 ($\pm$ 0.01), and

25.70 ($\pm$ 0.48) nm, respectively, at the end of equilibration with MD simulations. Values in

parentheses are standard deviations. The average density values of crystalline and non-crystalline

regions after MD equilibrations were 0.987 g/cm^3 and 0.853 g/cm^3, respectively. These are in

good agreement with bulk densities of 0.993 g/cm^3 and 0.847 g/cm^3 obtained with separate

simulations of PE in crystalline and amorphous phases, respectively, as well as those estimated from the experimental data.[17]

Effect of system size and crystallinity on stress-strain curves

Figure 3 (a) compares stress-strain curves obtained from deformation simulations with different system sizes, each having equal starting volumes of crystalline and non-crystalline regions, at the strain rate of 5×10^7 s^{-1}. The overall features of the stress-strain profiles are similar, indicating that no significant system size effect is present for tensile deformations with strains up to 0.49, at the strain rate of 5×10^7 s^{-1}. Figure 3 also shows stress-strain curves obtained with purely amorphous and crystalline phases of PE as described earlier. It should be noted that the initial, soft response observed up to a strain of 0.3 in the crystal simulation shown in Figure 3 (b) is indicative of fine crystallographic slip,[1,13] which is quite facile with the UA model of PE used here,[11] and results in reorientation of the chains in the crystal phase towards the direction of applied tensile strain; by a strain of 0.3, the chains are fully aligned in the tensile direction, and the response changes to deformation of the chains themselves. As expected, the stress-strain curve of the semicrystalline PE lies between the stress-strain curves obtained with amorphous and crystalline phases at larger strains. The Young's modulus of the fully amorphous PE was estimated to be about 30 MPa from the slope of the stress-strain curve with strains up to 0.05. We estimated the Young's modulus of crystalline PE to be 143 GPa from the slope of the linear fit of the stress-strain curve starting at a strain of 0.3 shown in Figure 3 (b), which is in reasonable agreement with experimental data and theoretical predictions,[31-33] considering that a united atom force field was used in our simulations instead of fully atomistic force fields.

Effects of extended strain range and different strain rates

With a bigger system size having increased lateral dimensions, we were able to perform deformation simulations over an extended strain range up to 1.23 (123%). Two strain rates of 5×10^7 s^{-1} and 5×10^6 s^{-1} were used, as in the previous study with smaller systems.[12] Representative snapshots and stress-strain curves for a representative starting configuration deformed at the two different strain rates are shown in Figures 4 and 5. This starting configuration (designated case #2) had one bridge segment with 349 UA sites. As illustrated in Figure 4, at the faster strain rate of 5×10^7 s^{-1}, the initially tilted crystalline stems gradually aligned with the strain direction until a peak at strain of 0.28. A cavity was observed in the non-crystalline region after the peak in tensile stress, and it grew bigger with increased strain. In contrast, little change was observed in the crystalline region in terms of the arrangement and packing of crystalline stems after the stress peak. As illustrated in Figure 5, at the slower strain rate of 5×10^6 s^{-1}, crystalline stems again aligned with the strain direction up to the peak in stress-strain curve, as was the case at the faster strain rate. However, no cavity formation was observed at the slower strain rate, as confirmed by the snapshots taken after the stress peak in Figure 5. Instead, multiple melting/recrystallization events were observed after the first stress peak, resulting in cyclic oscillations of stress that continued up to the strain of 1.23. Melting/recrystallization events were previously reported by Lee and Rutledge[11] and confirmed by Kim et al.,[12] but only with the larger strains employed here were multiple such events within a single system observed. At the later stages of tensile deformation, the crystalline region contained multiple crystalline domains, or grains, oriented at slightly different angles with respect to the direction of applied strain; thus, by the end of the deformation simulation, the crystalline domain is really a polycrystalline aggregate with several defects or grain boundaries within it, as shown in the last snapshot in Figure 5.

Figure 6 compares the ensemble-averaged stress-strain curves at the two different strain rates; these ensemble-averaged curves were obtained using runs starting from 100 different configurations. At the faster strain rate of 5×10^7 s^{-1}, the stress peaks around 108 MPa near a strain of 0.24, and then decreases monotonically. At the slower strain rate of 5×10^6 s^{-1}, the stress peaks around 90 MPa at a strain of 0.22, and then oscillates in a manner similar to that of the individual case shown in Figure 5. It is significant that the initial stress peak is lower at the slower strain rate, compared to the faster strain rate. This drop in yield stress with decreasing strain rate is in agreement with experimental and theoretical predictions[34-36] and would be consistent with a new yield mechanism that is activated at the slower strain rate; the intervention of this new mechanism precludes the accumulation of stress required to initiate cavitation. Post-yield, the magnitude of oscillation in stress is much lower after ensemble averaging. This reduction in magnitude of oscillations can be readily understood as the result of the less coherent nature of the cyclic responses among independent configurations within the ensemble. The result is a smoother stress-strain response that more closely mimics the plastic flow behavior observed experimentally in semicrystalline PE. However, we note that small oscillations persisted even after ensemble averaging over 100 configurations, representing diverse topological features in the non-crystalline region. We attribute this residual coherence of oscillations to the fact that our system comprises a single crystal lamella; a more realistic experimental sample would contain multiple lamellae with different thicknesses and orientations. Indeed, a smooth stress-strain response was observed in a recent simulation, using a coarse-grained model, of plastic deformation of a semicrystalline polyvinyl alcohol having small, randomly nucleated crystallites.[8] Finally, an increase of stress with increasing strain is observed at the later stages of deformation, indicating a strain hardening effect.

Changes in crystallinity and density during deformation

In tensile drawing of semicrystalline polymers, there is a competition between cavitation and activation of crystal plasticity.[37-40] To understand the structural transformations of semicrystalline PE in more detail, we analyzed the changes in crystallinity and density during the typical tensile deformations illustrated in Figures 4 and 5 (i.e. case #2). As shown in Figure 7 (a) and (b), during tensile deformation at the faster strain rate of 5×10^7 s^{-1}, the crystallinity changed very little, while density remained constant up to a strain of 0.2 and then decreased monotonically with additional strain. This behavior indicates that the crystallographic slip at strains below 0.2 allowed the system to contract laterally in response to tensile deformation, without sacrificing crystallinity; however, for strains larger than 0.2, the arrangement of the crystalline region remained more or less unchanged, as shown in the snapshots in Figure 4, while deformation was mostly localized in the non-crystalline region, resulting in cavitation. In contrast, at the slower strain rate, the crystallinity began to decrease significantly for strains above 0.2 and oscillated above a strain of 0.3, while the overall density also oscillated, in commensuration with the oscillations in crystallinity and stress, at values bounded by the amorphous and crystalline densities.

The middle and bottom rows of Figure 7 show profiles of the order parameter $P_{2,i}$ and the local density as a function of z position and strain, at the faster and slower strain rates, respectively. In these profiles, $z = 0$ was defined as the average z position (i.e. the mid-plane) of the non-crystalline region defined by the order parameter $P_{2,i}$. The thicknesses of the crystalline regions in the z direction during deformation, indicated by red and orange colors in the $P_{2,i}$ and density profiles, respectively, changed little with strain at the faster strain rate. However, at the slower strain rate, the thicknesses of the crystalline regions fluctuated and increased overall, but

"islands" of low $P_{2,i}$ order parameter and low local density became evident within the crystalline region, indicating grain boundaries and defects in a polycrystalline aggregate at the later stage of deformation, as described earlier. Figure 8 shows the number of crystal stems, lateral dimensions of the simulation cell, and densities in the crystalline and non-crystalline domains during the tensile deformations illustrated in Figures 4 and 5. We observed the displacement of polymer chains from crystalline to non-crystalline regions at the slower strain rate, as shown in Figure 8 (b). The number of crystal stems decreased stepwise in correlation with the observed oscillations in stress at the slower strain rate, while it remained constant at the faster strain rate as shown in Figure 8 (a). These changes in number of crystal stems were accompanied by corresponding reductions in lateral dimensions of the simulation cell at the slower strain rate as shown in Figure 8 (d). In contrast, lateral dimensions of the simulation cell changed very little at the faster strain rate, as shown in Figure 8 (c). These results indicate that the rearrangement of chains between crystalline and non-crystalline regions is the mechanism that precludes cavity formation at the slower strain rate. We also estimated local densities of crystalline and non-crystalline regions during deformations at the faster and slower strain rates as the average density within a slab with a thickness of 4 nm located at the mid-plane of the crystalline and non-crystalline regions, respectively. At the faster strain rate, the density in the crystalline region changed very little, while the density in the non-crystalline region declined significantly due to the expansion of the cavity as shown in Figure 8 (e). At the slower strain rate, densities in crystalline and non-crystalline regions oscillated during tensile deformations as shown in Figure 8 (f). When the density in the non-crystalline region is reduced with the increasing strain after the yield point, the chain segments occupying the crystalline domain move to the non-crystalline domain to compensate the reduced density in the non-crystalline domain. This results in the density

increase in the non-crystalline domain but destabilization, softening, and temporary melting in the crystalline domain with a sudden drop in the stress. It was observed that multiple chain segments in the crystalline domain moved nearly simultaneously to the non-crystalline domain, facilitated by the melting of the neighboring crystal stems. During the further straining, the crystalline domain reinforces itself with the remaining crystal stems, resulting in hardening and recrystallization in the crystalline domain and increase in stress, while the density in the non-crystalline domain begins to decline again. These melting/recrystallization processes were repeated during the entire extension deformation up to strain 1.23 at the slower strain rate.

In a small number of cases at the faster strain rate, we observed significant deviations from the average stress-strain curve, as shown in Figure 9. Figure 10 shows crystallinity and density profiles for case #53, illustrated in Figure 9 (c) and (g), which is chosen here because it showed the most deviation from the average stress-strain curve at the faster strain rate. At the slower strain rate, crystallinity and density for this case changed in a similar manner as those shown in Figure 7 for the representative case #2. However, at the faster strain rate, a significant change in crystallinity was observed during deformation, unlike the one shown in Figure 7. In addition, the overall density decreased until strain reached about 0.5 and then increased, indicating a decrease of cavity volume as shown in the local density profile in Figure 10 (d). Displacements of chain segments from crystalline to non-crystalline regions similar to those for case #2 at the slower strain rate (shown in Figure 8) were observed for case #53 at the faster strain rate, starting at strain of about 0.5. However, in all four cases shown in Figure 9, unlike the cases with the slower strain rate, cavitation preceded the displacements of chains, and no significant oscillatory behavior in stress-strain curve was observed. The volume of the cavity region decreased with the transport of chain segments from the crystalline region, resulting in

higher stresses compared to the average stresses at larger strains, as shown in Figure 9. These results indicate that there are two competing mechanisms reacting to the overall decrease in system density, cavity formation and transport of chains from crystalline to non-crystalline domains, which results in melting/recrystallization in the crystalline domain.

As a means of estimating crystalline stabilities during tensile deformation, we calculated the crystallinity and the $P_{2,i}$ in the crystalline region as a function of strain. These are shown in Figure 11 for the 4 individual cases shown in Figure 9, as well as the ensemble averaged values taken over all 100 configurations. The crystallinity averaged over 100 starting configurations increased slightly after the yield point at the faster strain rate. Compared to the average behavior, the crystalline regions in these 4 cases became less stable after the yield point, as indicated by lower crystallinities and smaller $P_{2,i}$ values even before the onset of the displacement of chains, which can facilitate the structural transformation in the crystalline region.

Effect of bridges and entanglements on stress-strain behavior

In addition to the change in crystallinity and density, topological features such as the bridge segment population in semicrystalline PE, illustrated in Figure 2, are believed to play an important role in the mechanical properties of semicrystalline PE, acting as physical, covalently-bonded "tie chains" between crystal lamellae. In the previous simulation study with a smaller system size,[12] only a small number of configurations containing a single bridge segment apiece (5 out of 10 configurations) were analyzed. One of our goals in this work was to prepare configurations with bigger system sizes, containing more diversity in the number of bridge segments per configuration. Figure 12 compares the average stress-strain curves obtained from the two sub-populations of the ensemble with and without bridge segments, respectively. At the

slower strain rate of 5×10^6 s^{-1}, the stress-strain behaviors compared in Figure 12 (b) are dominated by the oscillations associated with the rearrangement in the crystalline region, and the effect of bridge segments cannot be discerned readily. However, the stress-strain behavior at the strain rate of 5×10^7 s^{-1} in Figure 12 (a) shows that stress values beyond the peak position are higher with configurations containing bridges, indicating strain hardening.

Next we examined topological features of the four specific cases shown in Figure 9 that deviated significantly from the average stress-strain behavior at the faster strain rate of 5×10^7 s^{-1}. Table 1 summarizes the topological features such as bridge segments and entanglements at the beginning of deformation for these four cases. The starting configuration for the case shown in Figure 9 (a) (case #20) had the largest number of bridge segments (5) and included a bridge segment consisting of 185 UA sites, which is the shortest among all the bridge segments in our simulations (c.f. Table 1). This short bridge is thought to be responsible for the destabilization of the crystalline domain at the faster strain rate in this case, which allows displacement of chains similar to that observed more commonly at the slower strain rate. However, the bridge segment may not be the sole topological feature that influences the mechanical properties of semicrystalline PE, even though a certain degree of correlation was found as in the case of Figure 9 (a). Entanglements involving chain segments belonging to different crystalline regions, called "bridging entanglements",[12] can play a role in the mechanical properties of semicrystalline PE during tensile deformations. For example, the configuration for Figure 9 (b) (case #30) contained only two bridge segments but had the largest number of loop-loop bridging entanglements (6), as shown in Table 1. One of these bridging entanglements may have been responsible for triggering the destabilization of the crystalline domain. The configuration for Figure 9 (d) (case #100), which displays a stress-strain curve that significantly deviates from the

18

average, did not have any bridge segment but had the shortest entanglement length $N_{e,\text{coil}}$ in the non-crystalline region out of all 100 configurations. This indicates that entanglements indeed play an important role during tensile deformations.

Table 2 shows the overall changes of entanglement statistics during tensile deformations. $\langle \bar{Z}_{sc} \rangle$, the average number of entanglements in the whole system, including both crystalline and non-crystalline regions, declined 5% on average during tensile deformation at the faster strain rate of 5×10^7 s^{-1}. By contrast, $\langle \bar{Z}_{sc} \rangle$ increased 8% during deformation at the slower strain rate of 5×10^6 s^{-1}. This difference can be traced to changes in the crystallinity of semicrystalline PE during tensile deformations at the two strain rates. As shown in Figure 11, at the faster strain rate, when averaged over 100 configurations, the crystallinity increases slightly after the yield point. This is partly due to the artifact of aligned chain segments near the cavity, which affect the order parameter used to measure crystallinity and, like crystalline segments, are unlikely to be entangled. In contrast, at the slower strain rate, during repeated melting/recrystallization transitions, the crystallinity decreases, as shown in Figure 7 (a), resulting in an increase of non-crystalline sites, and thus more entanglements. Lee and Rutledge[11] also found that the number of entanglements correlates strongly with the fraction of non-crystalline material within the semicrystalline phase of PE. Table 2 also shows the changes of $\langle \overline{N}_{e,\text{coil}} \rangle$ and $\langle \overline{N}_{e,\text{kink}} \rangle$ in the non-crystalline region at the faster strain rate of 5×10^7 s^{-1}, where overbar and angle bracket signify averages over chains in each configuration and over the ensemble of configurations, respectively. Both $\langle \overline{N}_{e,\text{coil}} \rangle$ and $\langle \overline{N}_{e,\text{kink}} \rangle$ increased during the deformation, which is consistent with the overall decrease of $\langle \bar{Z}_{sc} \rangle$ at the faster strain rate. The changes of $N_{e,\text{coil}}$ in the non-crystalline region and in the numbers of loop-loop, loop-tail, and tail-tail bridging entanglements are shown in Figure 13. As shown in Tables 1 and 2 and Figure 13, in the beginning of the deformation, $\langle \overline{N}_{e,\text{coil}} \rangle$ in

the non-crystalline region was 27.9, which is significantly lower than experimental estimates of 59 and 82 for PE in the melt state at 413 K[41] and 450 K,[42] respectively. This discrepancy is mainly due to polydispersity of segment lengths in the non-crystalline domain and the presence of many chain segments that are shorter than the average entanglement length $\langle \overline{N}_{e,\text{coil}} \rangle$. To examine this bias due to short chain segments, we calculated $\langle \overline{N}_{e,\text{coil}} \rangle$ using a larger cutoff in segment length. With chain segments longer than 100 UA sites, $\langle \overline{N}_{e,\text{coil}} \rangle$ was found to be about 83±13, which is in good agreement with that calculated for bulk amorphous PE using a different UA force field.[29] As shown in Figure 13 (a), for all four cases in Figure 9, $\overline{N}_{e,\text{coil}}$ values at the end of deformation were lower than the overall average $\langle \overline{N}_{e,\text{coil}} \rangle$, indicating more entangled states with increased non-crystalline sites as a result of the decreased crystallinity. The case #100 represented in Figure 9 (d) that had the smallest $\overline{N}_{e,\text{coil}}$ in the beginning had the smallest $\overline{N}_{e,\text{coil}}$ at the end as well. $\overline{N}_{e,\text{coil}}$ values for the case #20 represented in Figure 9 (a) were larger than the average in the beginning but smaller than the average at the end of deformation. The number of bridging entanglements n_{be} was also analyzed and is summarized in Table 1 and Figure 13. Overall, n_{be} decreased with increasing tensile deformation. However, some bridging entanglements persisted during tensile deformations. For instance, the case represented in Figure 9 (c) (case #53), which displays the most deviation from the average stress-strain curve, had 39 bridging entanglements remaining in the non-crystalline region at the end of deformation, as illustrated in Figure 13 (b). This number is significantly larger than the average value of 20.3 and is the second largest among 100 cases. These persistent bridging entanglements can influence the stress-strain behaviors of semicrystalline PE by pulling chains from crystalline into non-crystalline regions. In most cases at the faster strain rate, PE stems in the crystal domain were found to slide along their length through an α_c relaxation process[11,43] while maintaining the total

number of stems in the crystalline domain. However, in small number of cases, certain movements, such as concerted pulling by multiple bridging entanglements or strong entanglement on one side coupled with short tail or loop on the other side, could induce disruptions in the crystalline region during tensile deformations, resulting in deviations from the average stress-strain behavior as shown in Figure 9.

Deformations at a lower temperature

If interactions between crystal stems are strong enough, the crystalline domain could remain intact despite the topological constraints. To test this hypothesis, we performed tensile deformation simulations at the lower temperature of 250 K at the slower strain rate of 5×10^6 s^{-1} as well as at the faster strain rate of 5×10^7 s^{-1}. This temperature is slightly higher than the glass transition temperature T_g of 220 K[22] estimated for PE with the same force field. However, recent work by Brown and co-workers[34,44] indicates that the full stress-strain response for high density polyethylene (HDPE) in compression follows a linear time-temperature superposition with a 1 decade increase in strain rate being approximately equivalent to a 10 K drop in temperature. Thus, a strain rate on the order of 10^6 s^{-1} is expected to give rise to a glassy response in semicrystaline PE, in contrast to the melt-like response expected, and observed, for the non-crystalline domain at 350 K. Stress-strain curves obtained at 250 K are shown in Figure 14. Indeed, we confirmed that cavity formation, instead of melting/recrystallization, re-emerges as the dominant mechanism, even at the slower strain rate, when the temperature is lowered and the liquid-like response required for melting/recrystallization events is suppressed. In addition, yield stress values at 250 K are higher than the corresponding values at 350 K, in agreement with experimental and theoretical predictions.[34]

Summary

We studied tensile deformations of semicrystalline polyethylene with molecular dynamics simulations at the two different strain rates of 5×10^7 s^{-1} and 5×10^6 s^{-1}. The competition between the thermodynamic stability of the crystalline region and the displacement of polymer chains from crystalline to non-crystalline regions plays an important role in structural transformations of semicrystalline PE during tensile deformations. At the faster strain rate, yield is accompanied by cavitation in the non-crystalline region, with little change in the crystalline region except in a few atypical cases. This mechanism results in monotonically declining stress values in the stress-strain curve post-yield. However, topological constraints such as bridges and bridging entanglements connecting crystalline lamellae could still induce destabilization of the crystalline lamellae, and significant rearrangements of chains between crystalline and non-crystalline regions and deviations from the average stress-strain behavior were observed even at the faster strain rate in a small number of cases. At the slower strain rate, the displacement of entire stems from crystalline to non-crystalline regions was sufficient to suppress cavitation, and correlated with multiple melting/recrystallization events and significant oscillations of stress, crystallinity, and density. However, when averaged over an ensemble of independent starting configurations of semicrystalline PE, the stress increased gradually with the increased strain, indicating a strain hardening effect. These distinct stress-strain behaviors observed at the two different strain rates indicate that there exists a critical strain rate that separates deformation regimes with different mechanisms for yield and plastic response. Indeed, such a separation into regimes with and without cavity formation, depending on strain rate, has been observed experimentally.[37] However, the critical strain rate is expected to depend on various conditions such as the temperature and the thickness of the crystalline region, precluding a direct comparison to experiment. Nevertheless, it seems apparent from these simulations that the

displacement of crystal stems from the crystalline region is a key process that may determine this critical strain rate. Further investigation is required to quantify the rate-dependence and activated nature of this process. For a more general understanding of the stress-strain behaviors, we plan to characterize mechanical and structural properties of semicrystalline PE with different crystallinities, other deformation modes, and more realistic force fields in close connection with experimental results.
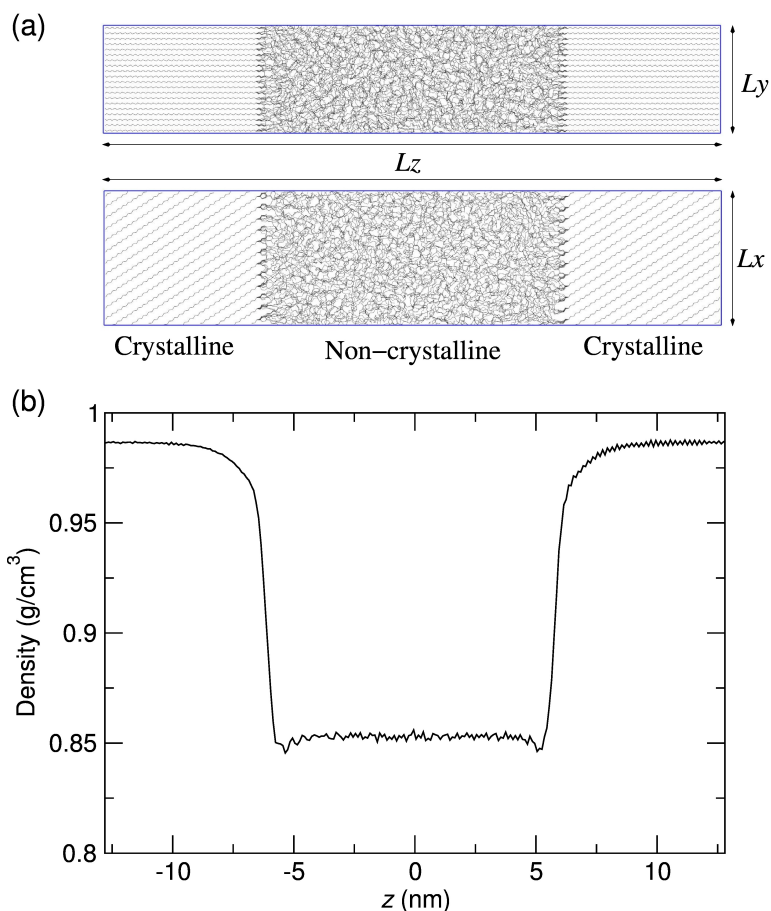
Figure 1. (a) Schematics of the simulation set-up for semicrystalline PE. The top and bottom images are views along the *x* and *y* axes, respectively. During simulation, periodic boundary conditions are applied in all directions. L_x, L_y, and L_z are the lengths of the simulation cell in *x*, *y*, and *z* directions, respectively. As evident in the lower image, the chains in the crystal are tilted about 34° with respect to the lamellar stack direction (*z*-direction), so that the {201} crystallographic plane of the crystalline region of PE is normal to the *z* direction.

(b) Profile of mass density along the *z* direction, obtained from constant pressure molecular dynamics (MD) simulations. The density was calculated from the analysis of the final 4 ns of 8-ns *NPT* simulations, averaged over runs with 100 starting configurations.
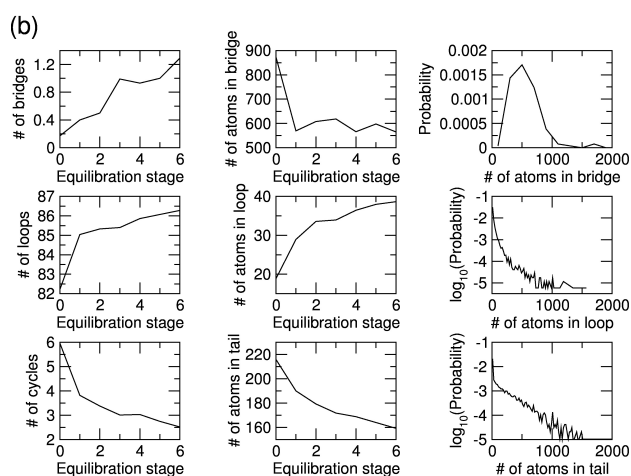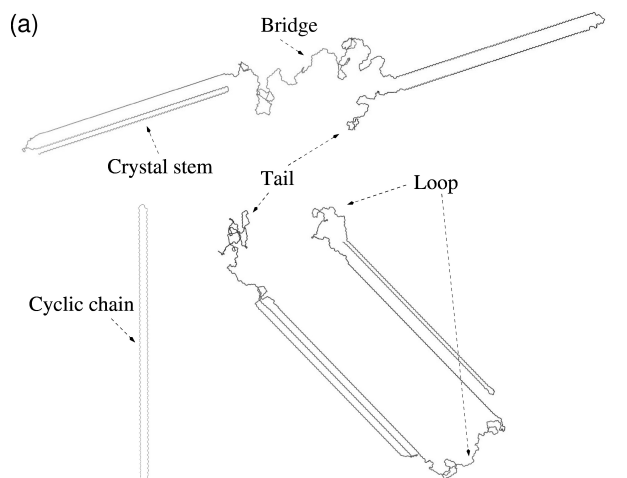
Figure 2.(a) Illustration of loop, tail, bridge segments and cyclic chains. Cyclic chains containing two or more crystal stems can be formed, as illustrated here. (b) Evolution of topological features during IMC equilibration. The equilibration stage 0 signifies IMC equilibration at 10000 K with 10000 MC cycles. Equilibration stages 1 through 6 signify 6 consecutive sessions of IMC simulation at T= 350 K. Left-most panels show the average number of bridges (top), loops (middle), and cyclic chains (bottom) in each configuration. Center panels show the total number of atoms in each bridge (top), loop (middle), and tail (bottom) segment. Right-most panels show probability distributions of number of atoms in each bridge (top), loop (middle), and tail (bottom) segment after IMC equilibration.
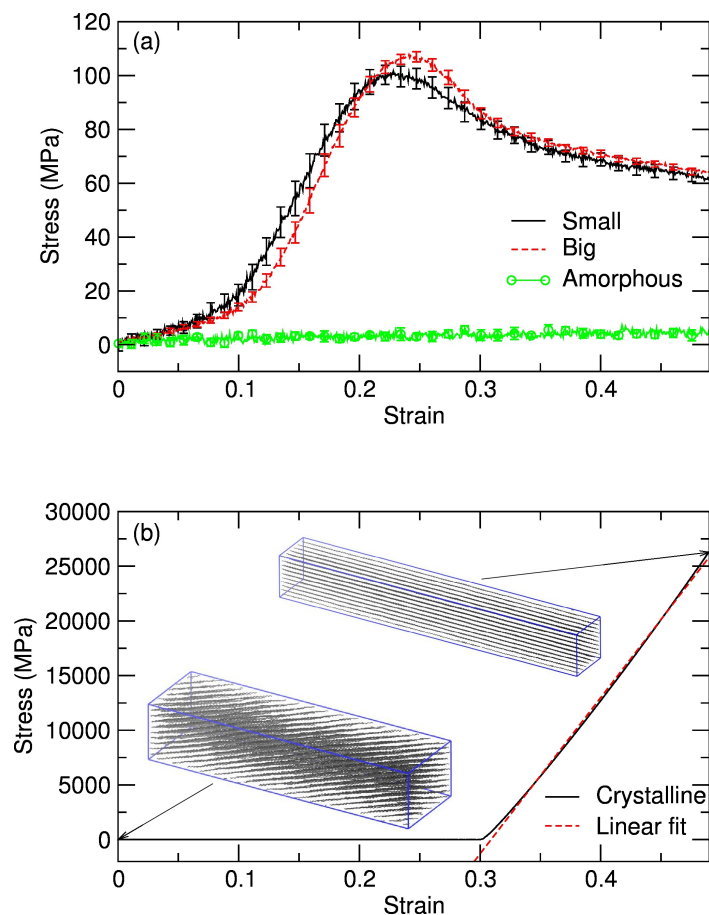
Figure 3. (a) Comparison of stress-strain curves with different system sizes. Simulations with smaller (solid line) and larger (dashed line) system sizes contained 5556 and 26664 united-atom sites, respectively. Error bars in average stress-strain curves reported in this and following figures were estimated as 1.96 times the standard error, based on the 95% confidence interval. The line with circles represents the result from bulk simulations of amorphous PE. (b) The stress-strain curve of the crystalline PE is shown with a solid line. The dashed line represents a linear fit of the stress-strain curve in the range beyond that where fine crystallographic slip occurs, which was used to estimate the Young's modulus of the crystalline PE. The snapshots inside the plot illustrate initial and final configurations during the tensile deformation of the crystalline PE system.
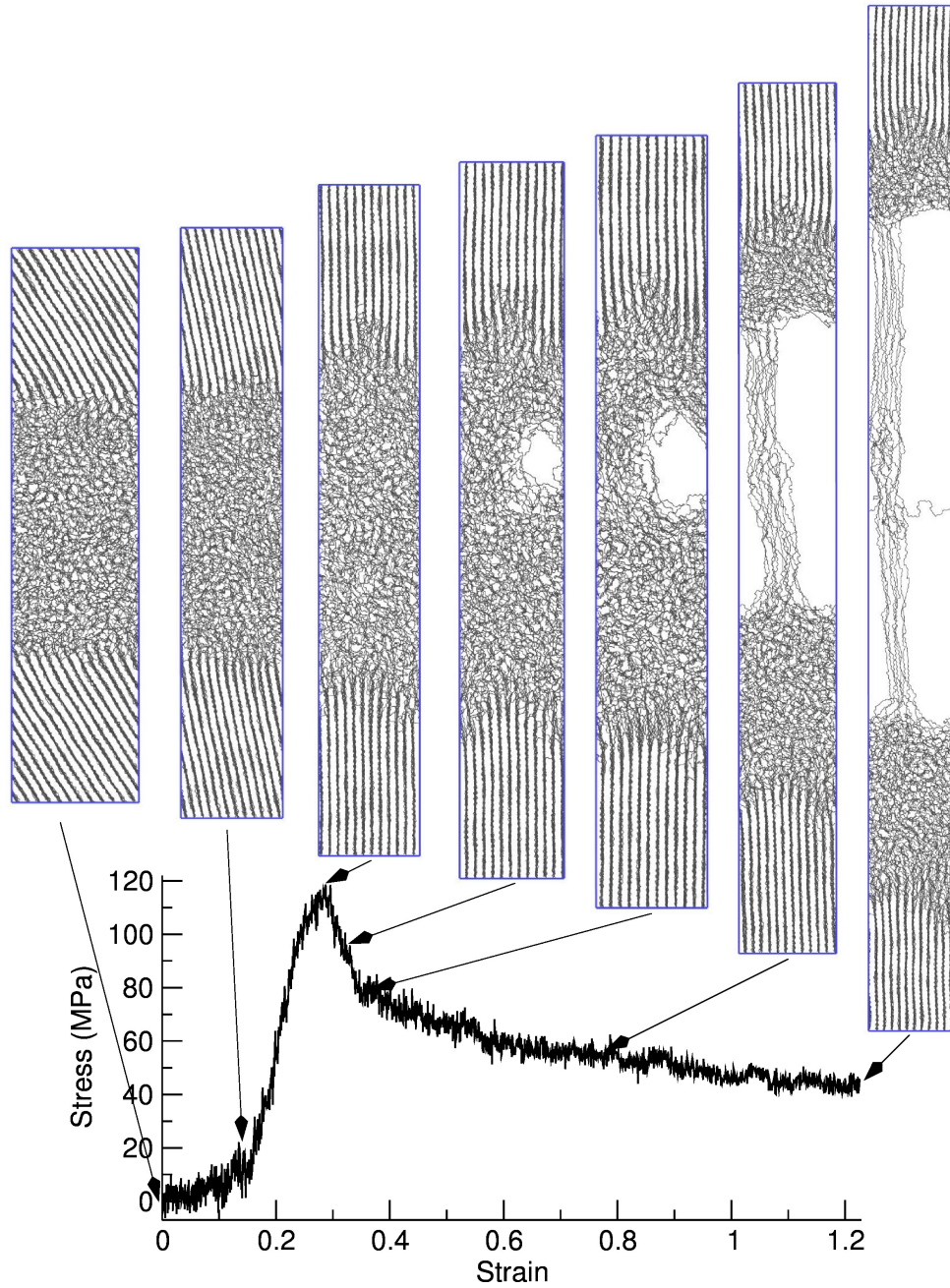
Figure 4. Snapshots of semicrystalline PE and the corresponding stress-strain curve during a faster deformation (strain rate of 5×10^7 s^{-1}) from a representative configuration (denoted case #2).
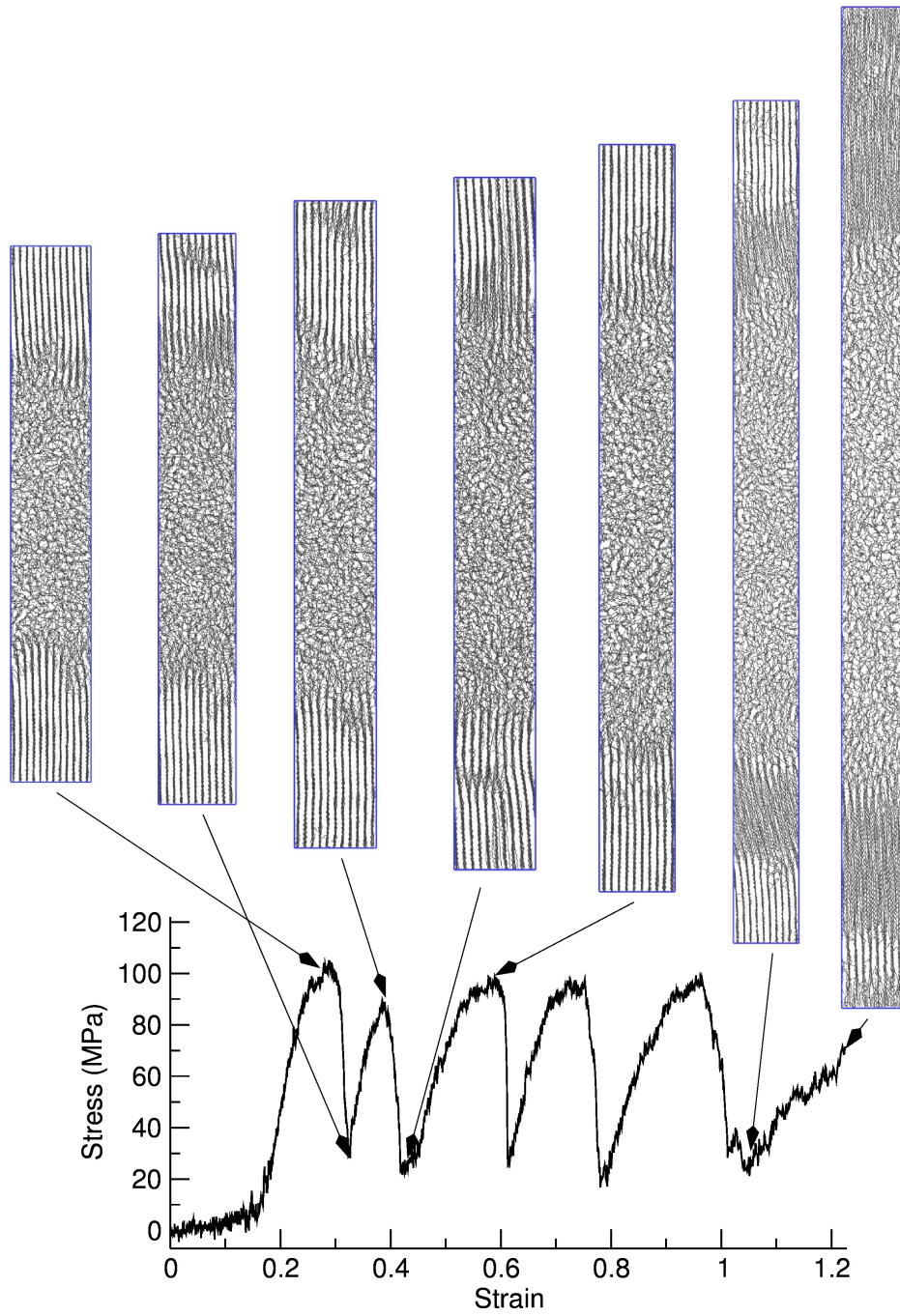
Figure 5. Snapshots of semicrystalline PE and the corresponding stress-strain curve during a slower deformation (strain rate of 5×10^6 s^{-1}) starting with the same representative configuration in Figure 4.
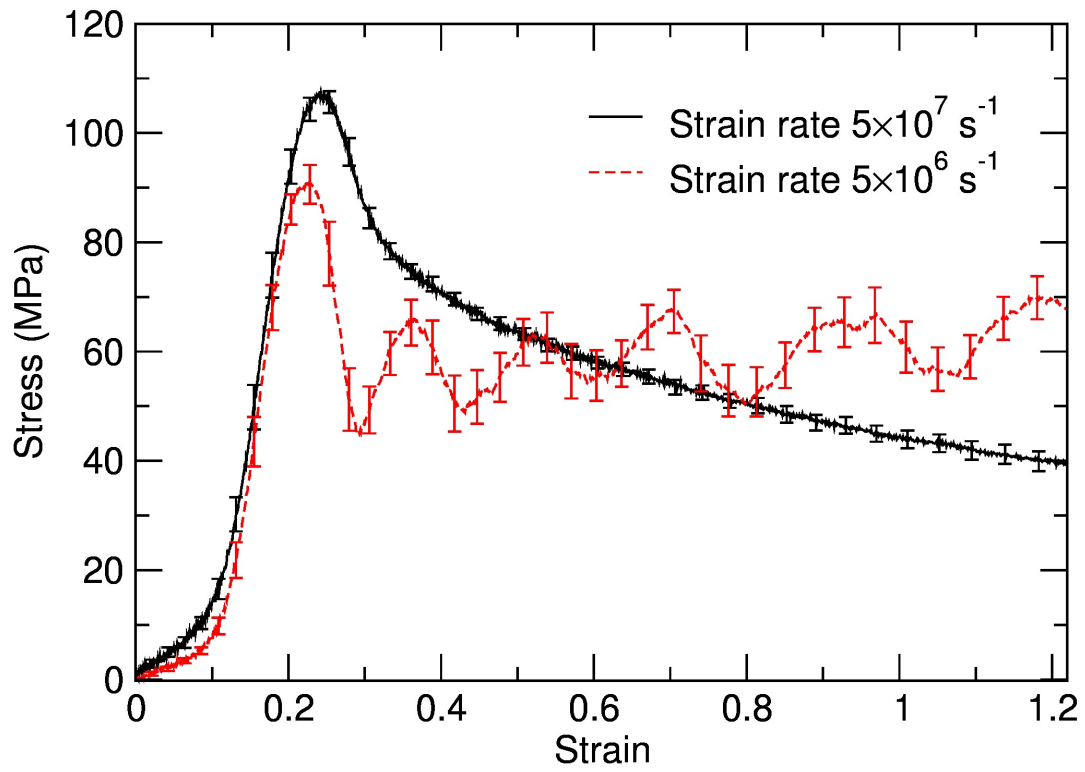
Figure 6. Stress-strain curves with faster and slower strain rates shown as solid and dashed lines, respectively, averaged over the ensembles with 100 different starting configurations.
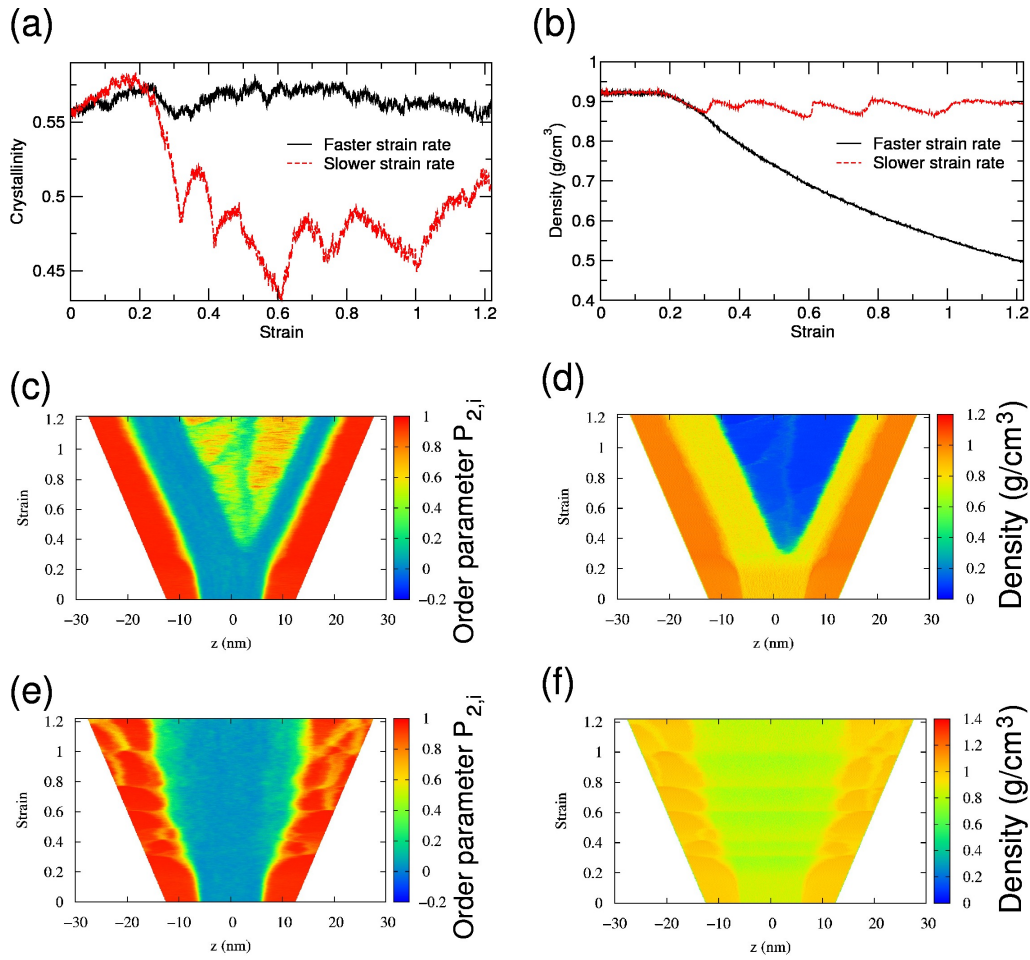
Figure 7. (a) Crystallinities and (b) overall densities as a function of strains during tensile deformations of the representative configuration (case #2) illustrated in Figures 4 and 5, at two different strain rates of 5×10^7 s^{-1} and 5×10^6 s^{-1} represented with solid and dashed lines, respectively. Profiles of (c) order parameter $P_{2,i}$ and (d) density are shown as a function of z position and strain with the faster strain rate of 5×10^7 s^{-1}. (e) and (f) show similar profiles of $P_{2,i}$ and the density, respectively, at the slower strain rate of 5×10^6 s^{-1}. $z=0$ corresponds to the center of the non-crystalline region.
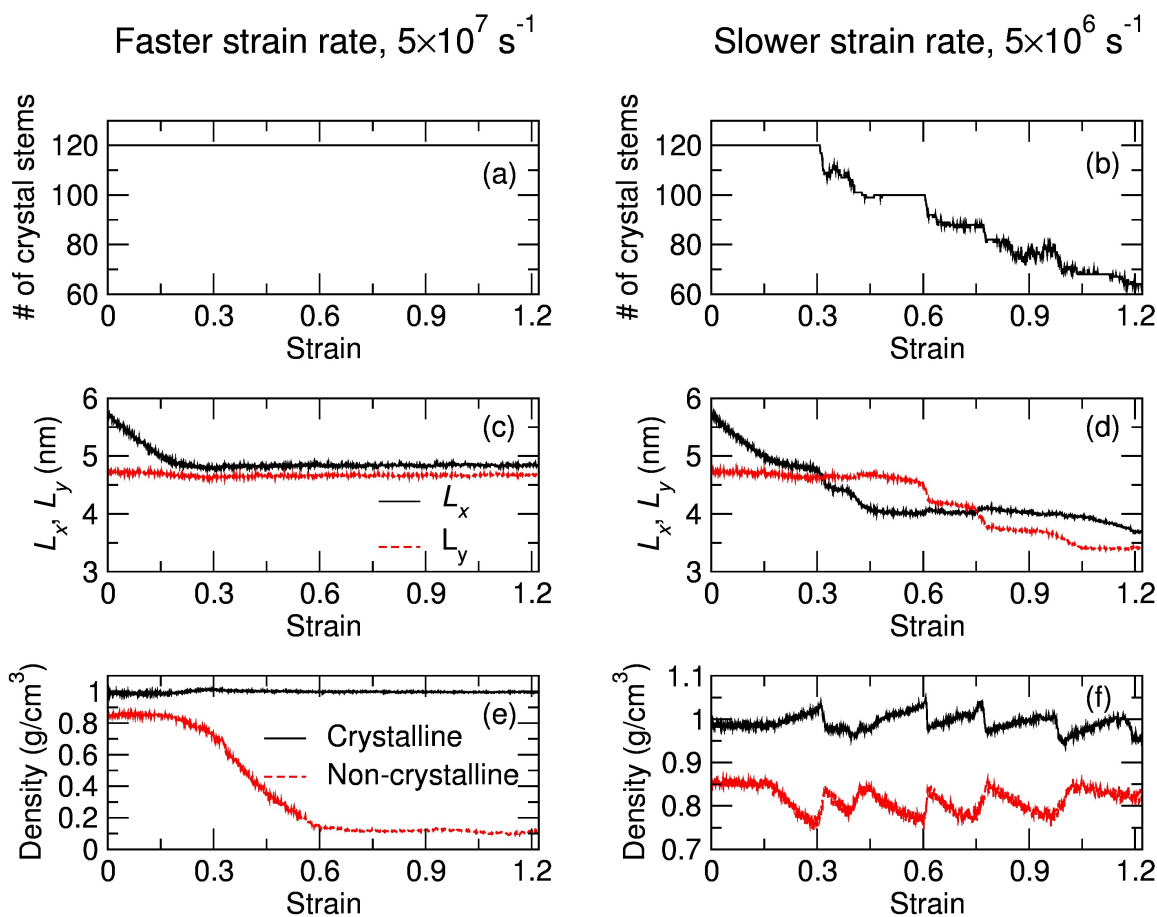
Figure 8. Number of chain stems in the crystalline region at (a) faster and (b) slower strain rates during typical tensile deformations illustrated in Figures 4 and 5. Lengths of the simulation cell in x and y directions, L_x (black line) and L_y (red line), respectively, during deformations at (c) faster and (d) slower strain rates. Densities of crystalline (black line) and non-crystalline (red line) regions within the z distance of 2 nm from the respective centers at (e) faster and (f) slower strain rates.
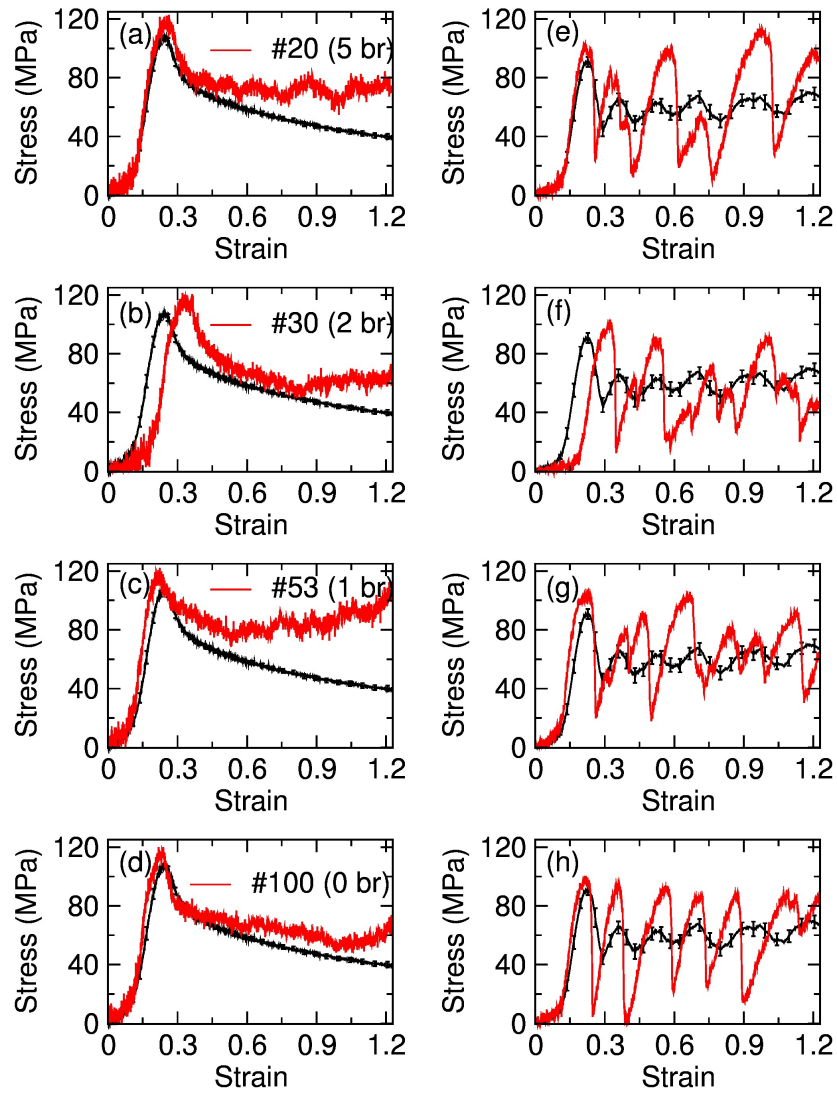
Figure 9. Red lines in the plots on the left (a, b, c, and d) show stress-strain curves for four individual cases that deviated significantly from the ensemble averaged stress-strain curve (black lines, reproduced from Fig 6) at the faster strain rate of 5×10^7 s^{-1}. The plot on the right (e, f, g, and h) in each row shows the corresponding result at the slower strain rate with the same starting configuration as the one to its left with a red line along with the ensemble averaged stress-strain curve shown with a black line (also reproduced from Fig 6).
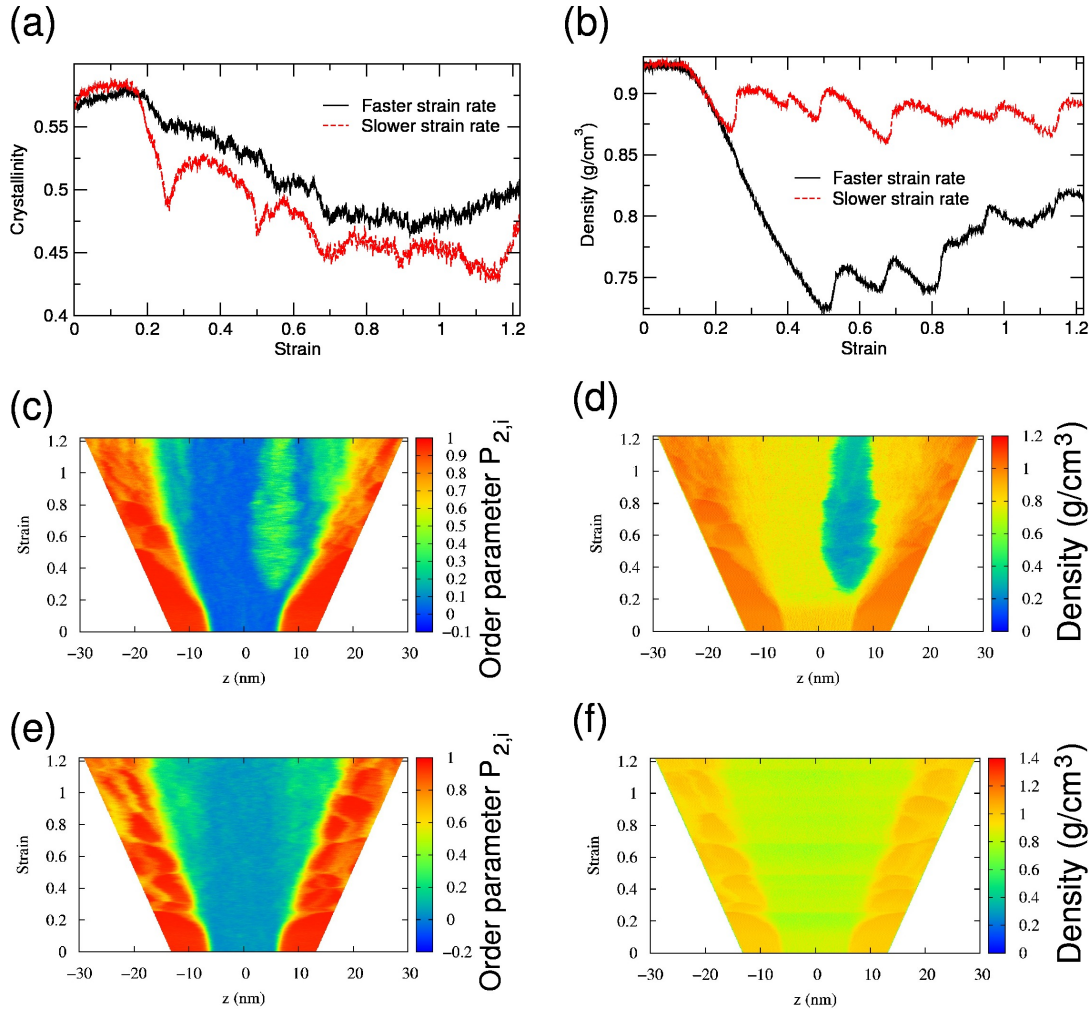
Figure 10. (a) Crystallinities and (b) overall densities as a function of strains during tensile deformations from the initial configuration corresponding to the case #53 shown in Figure 9 (c) and (g), which displays the most deviation from the average stress-strain curve at the strain rate of 5×10^7 s^{-1}. The results at two different strain rates of 5×10^7 s^{-1} and 5×10^6 s^{-1} are compared with solid and dashed lines, respectively. Profiles of (c) order parameter $P_{2,i}$ and (d) density are shown as a function of z position and strain at the faster strain rate of 5×10^7 s^{-1}. (e) and (f) show similar profiles of $P_{2,i}$ and the density, respectively, at the slower strain rate of 5×10^6 s^{-1}.
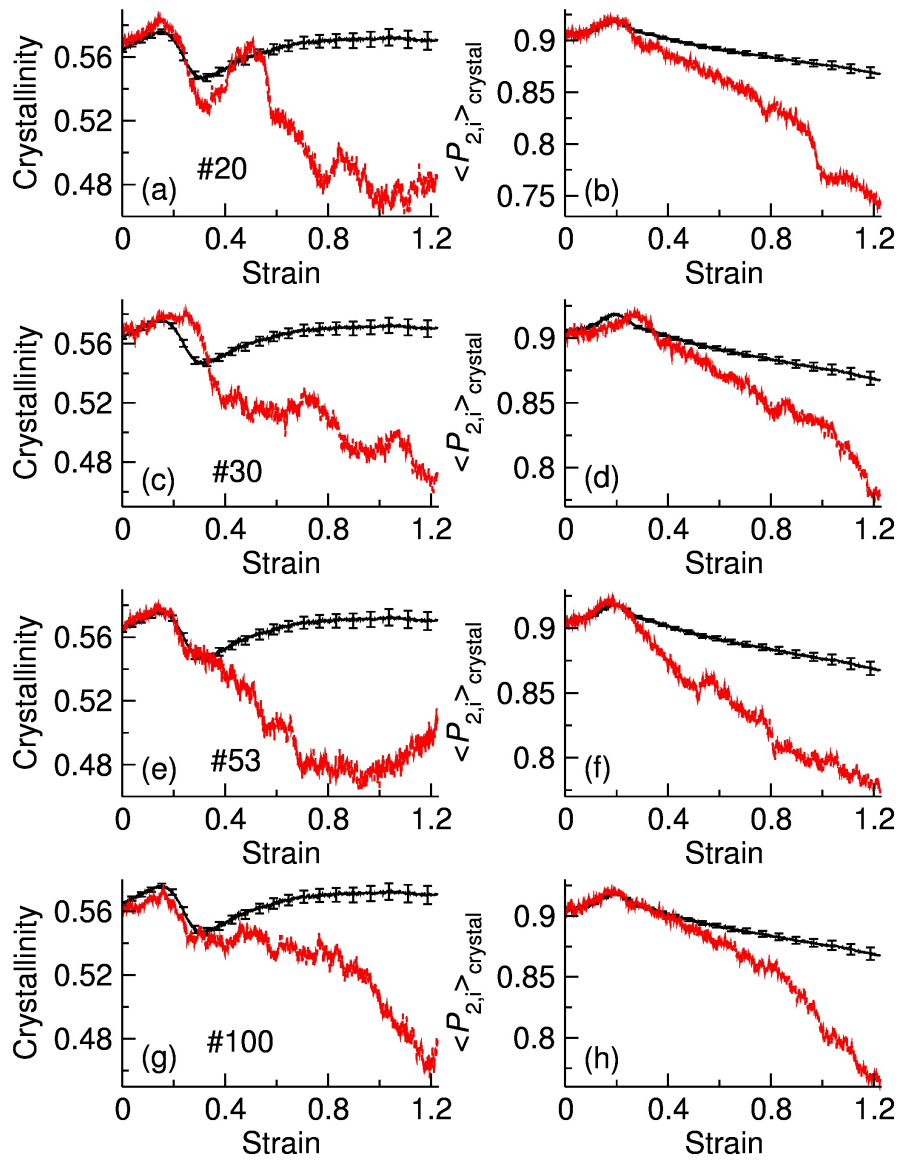
Figure 11. The crystallinities (a, c, e, and g) and the order parameters (b, d, f, and h) evaluated just in the crystalline region as a function of strain. Red lines: the four specific cases, shown in Figure 9, that display stress-strain behaviors deviating from the ensemble average, at the faster strain rate. Black lines: the ensemble-averaged values over all 100 configurations.
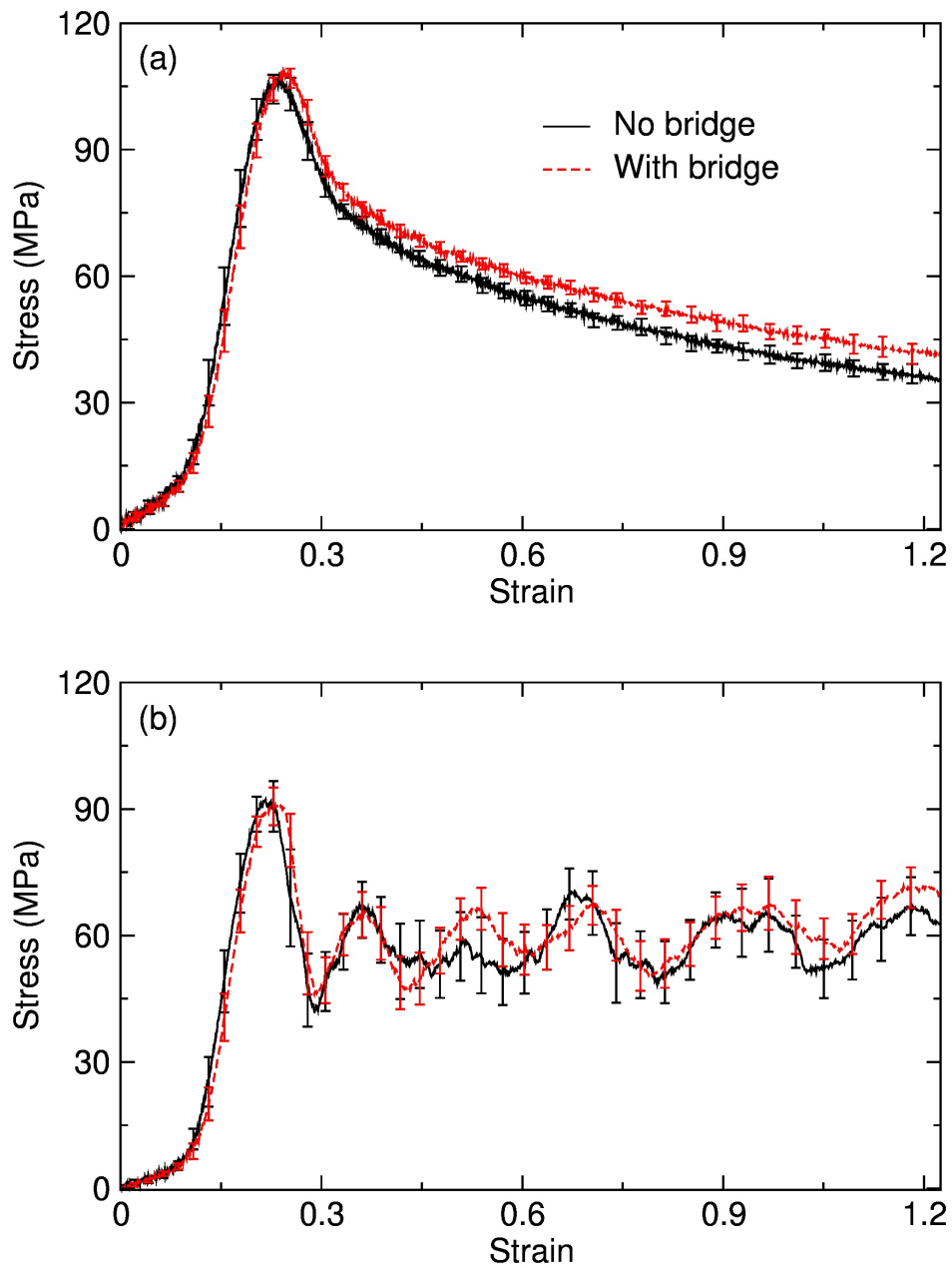
Figure 12. Effect of bridge segments on stress-strain curves at (a) faster and (b) slower strain rates. Solid and dashed lines represent the stress-strain curves averaged over the 34 configurations without bridges and the 66 configurations with bridges, respectively.
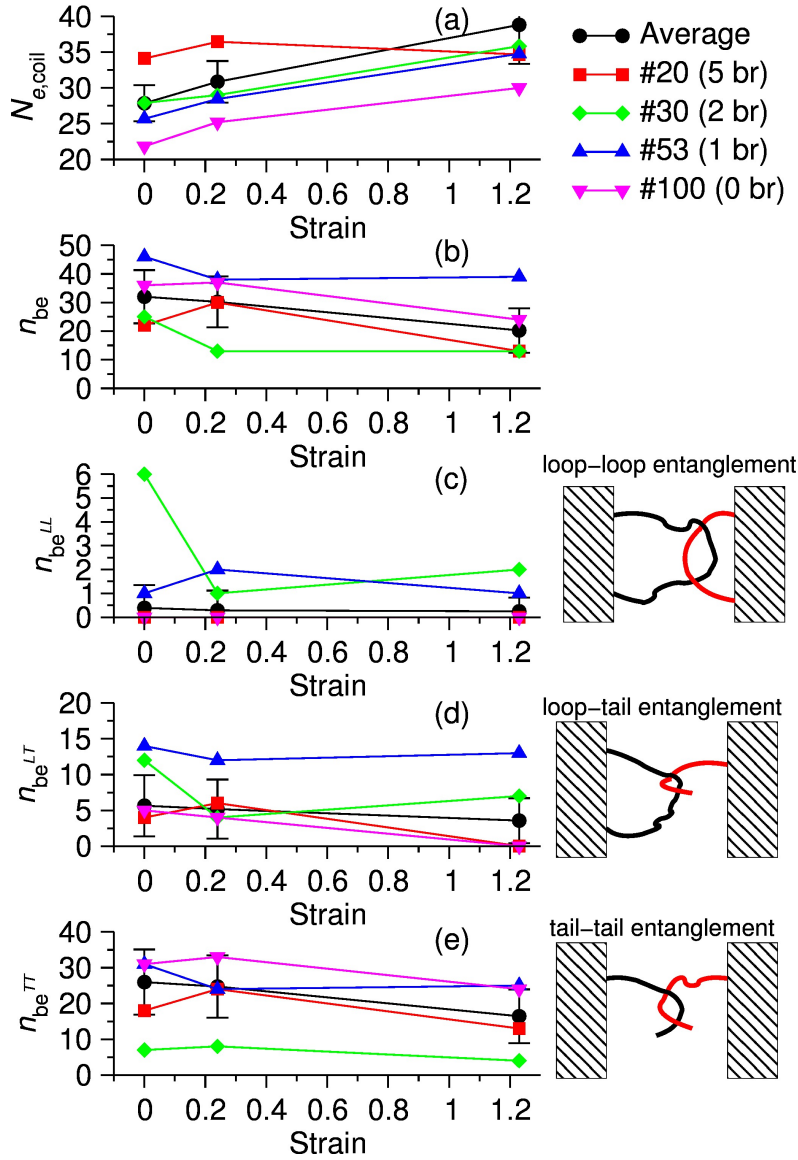
Figure 13. Change of entanglement statistics during tensile deformations at the faster strain rate of 5×10^7 s^{-1}. (a) shows entanglement length $N_{e,\text{coil}}$. (b), (c), (d), and (e) show the numbers of total, loop-loop, loop-tail, and tail-tail bridging entanglements, respectively. Lines with circles represent the data averaged over all 100 configurations. Lines with squares, diamonds, triangles, and inverted triangles represents the results corresponding the cases in Figure 9 (a), (b), (c), and (d), respectively. Uncertainties were estimated with standard deviations.
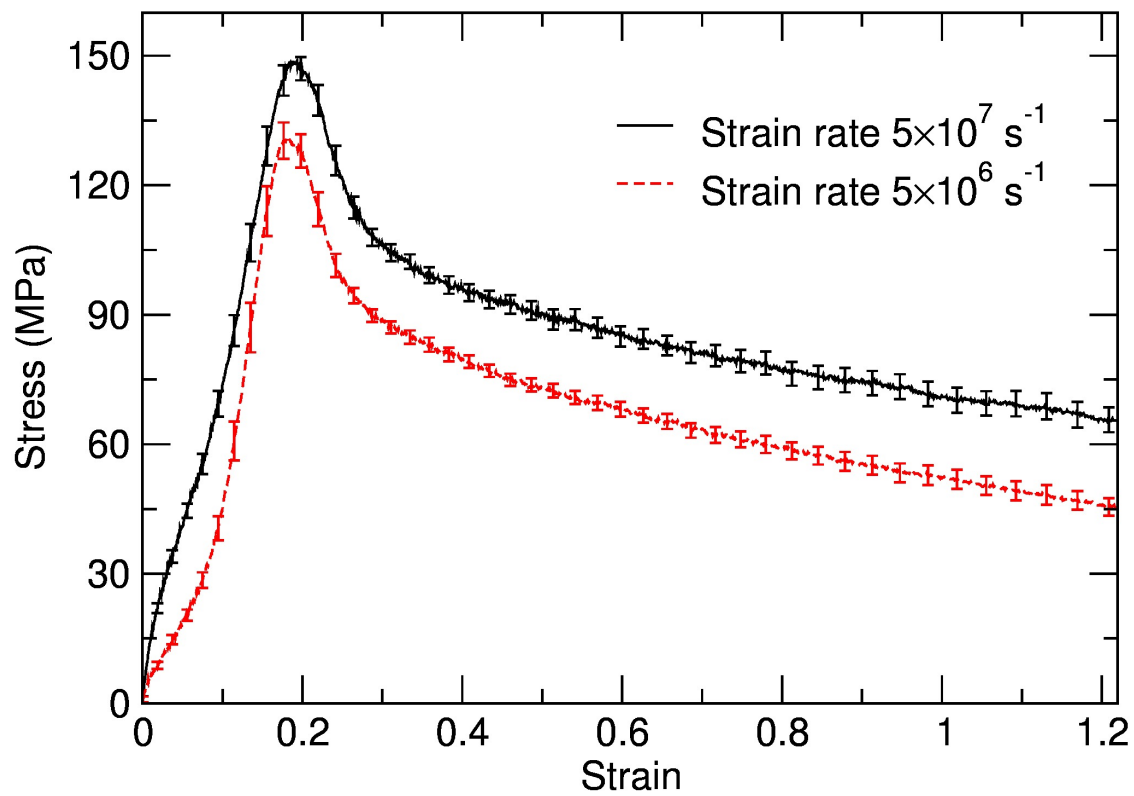
Figure 14. Stress-strain curve from tensile deformation simulations at 250 K with the strain rates of 5×10^7 s^{-1} (solid line) and 5×10^6 s^{-1} (dashed line).

Table 1. Summary of topological features existing at the beginning of tensile deformations.

Overbar in $\overline{N}_{e,\text{coil}}$ signifies an average over chains in each configuration.

| | $\overline{N}_{e,\text{coil}}$ | n_{be}, number of bridging entanglements | | | | no. of bridges | no. of UA atoms in shortest bridge |
		total	loop-loop	loop-tail	tail-tail		
average	27.9	32	0.4	5.6	26	1.29	445
#20	34.1	22	0	4	18	5	185
#30	27.9	25	6	7	12	2	315
#53	25.7	46	1	14	31	1	285
#100	21.9	36	0	5	31	0	N/A

Table 2. Change of entanglement statistics during tensile deformations. Uncertainties were estimated with standard deviations. Fast and slow strain rates refer to 5×10^7 s^{-1} and 5×10^6 s^{-1}, respectively. The overall average number of entanglements $\langle\bar{Z}_{sc}\rangle$ calculated using the whole system, including both crystalline and non-crystalline regions, is normalized by its initial value $\langle\bar{Z}_{sc}\rangle_0$. $\langle\bar{N}_{e,\text{coil}}\rangle$ and $\langle\bar{N}_{e,\text{kink}}\rangle$ were calculated from chain segments in the non-crystalline region only. Overbar and angle bracket signify averages over chains in each configuration and over the ensemble of configurations, respectively.

	Strain rate	Strain		
		0	0.24	1.23
$\langle\bar{Z}_{sc}\rangle/\langle\bar{Z}_{sc}\rangle_0$	Fast	1	0.99±0.04	0.95±0.06
	Slow			1.08±0.10
$\langle\bar{N}_{e,\text{coil}}\rangle$	Fast	27.9±2.5	30.9±2.9	38.8±5.4
$\langle\bar{N}_{e,\text{kink}}\rangle$	Fast	18.0±1.1	19.8±1.4	23.3±2.5

AUTHOR INFORMATION

Corresponding Authors

*E-mail: jan.w.andzelm.civ@mail.mil (J.W.A.) and rutledge@mit.edu (G.C.R).

ACKNOWLEDGMENT

REFERENCES

(1)   Galeski, A. *Prog. Polym. Sci.* **2003**, *28*, 1643.

(2)   Chen, X.; Yoon, K.; Burger, C.; Sics, I.; Fang, D.; Hsiao, B. S.; Chu, B. *Macromolecules* **2005**, *38*, 3883.

(3)   Litvinov, V. M.; Xu, J.; Melian, C.; Demco, D. E.; Möller, M.; Simmelink, J. *Macromolecules* **2011**, *44*, 9254.

(4)   Flory, P. J. *J. Am. Chem. Soc.* **1962**, *84*, 2857.

(5)   Keller, A. *Philos. Mag.* **1957**, *2*, 1171.

(6)   Queyroy, S.; Monasse, B. *Int. J. Multiscale Com.* **2011**, *9*, 119.

(7)   Queyroy, S.; Monasse, B. *J. Appl. Polym. Sci.* **2012**, *125*, 4358.

(8)   Jabbari-Farouji, S.; Rottler, J.; Lame, O.; Makke, A.; Perez, M.; Barrat, J.-L. *ACS Macro Letters* **2015**, *4*, 147.

(9)   Balijepalli, S.; Rutledge, G. C. *J. Chem. Phys.* **1998**, *109*, 6523.

(10)   in 't Veld, P. J.; Hütter, M.; Rutledge, G. C. *Macromolecules* **2006**, *39*, 439.

(11)   Lee, S.; Rutledge, G. C. *Macromolecules* **2011**, *44*, 3096.

(12)   Kim, J. M.; Locker, R.; Rutledge, G. C. *Macromolecules* **2014**, *47*, 2515.

(13)   Lin, L.; Argon, A. S. *J Mater Sci* **1994**, *29*, 294.

(14)	In *http://sourceforge.net/projects/montecarlo/*.

(15)	in 't Veld, P. J.; Rutledge, G. C. *Macromolecules* **2003**, *36*, 7358.

(16)	Paul, W.; Yoon, D. Y.; Smith, G. D. *J. Chem. Phys.* **1995**, *103*, 1702.

(17)	Mark, J. E. *Polymer Data Handbook (2nd Edition)*; Oxford University Press.

(18)	Gautam, S.; Balijepalli, S.; Rutledge, G. C. *Macromolecules* **2000**, *33*, 9136.

(19)	Chang, J.; Han, J.; Yang, L.; Jaffe, R. L.; Yoon, D. Y. *J. Chem. Phys.* **2001**, *115*, 2831.

(20)	Plimpton, S. *J. Comput. Phys.* **1995**, *117*, 1.

(21)	Shinoda, W.; Shiga, M.; Mikami, M. *Phys. Rev. B* **2004**, *69*, 134103.

(22)	Yi, P.; Locker, C. R.; Rutledge, G. C. *Macromolecules* **2013**, *46*, 4723.

(23)	Sun, H. *J. Phys. Chem. B* **1998**, *102*, 7338.

(24)	Yi, P.; Rutledge, G. C. *J. Chem. Phys.* **2011**, *135*.

(25)	Hoy, R. S.; Robbins, M. O. *Phys. Rev. E* **2005**, *72*, 061802.

(26)	Sussman, D. M.; Tung, W.-S.; Winey, K. I.; Schweizer, K. S.; Riggleman, R. A. *Macromolecules* **2014**, *47*, 6462.

(27)	Kröger, M. *Comput. Phys. Commun.* **2005**, *168*, 209.

(28)	Everaers, R.; Sukumaran, S. K.; Grest, G. S.; Svaneborg, C.; Sivasubramanian, A.; Kremer, K. *Science* **2004**, *303*, 823.

(29)	Hoy, R. S.; Foteinopoulou, K.; Kröger, M. *Phys. Rev. E* **2009**, *80*, 031803.

(30)	Foteinopoulou, K.; Karayiannis, N. C.; Mavrantzas, V. G.; Kroger, M. *Macromolecules* **2006**, *39*, 4207.

(31)	Matsuo, M.; Sawatari, C. *Macromolecules* **1986**, *19*, 2036.

(32)	Lacks, D. J.; Rutledge, G. C. *J. Phys. Chem.* **1994**, *98*, 1222.

(33)	Li, P.; Hu, L.; McGaughey, A. J. H.; Shen, S. *Adv. Mater.* **2014**, *26*, 1065.

(34)	Furmanski, J.; Cady, C. M.; Brown, E. N. *Polymer* **2013**, *54*, 381.

(35)	Richeton, J.; Ahzi, S.; Daridon, L.; Rémond, Y. *Polymer* **2005**, *46*, 6035.

(36)	Richeton, J.; Ahzi, S.; Vecchio, K. S.; Jiang, F. C.; Adharapurapu, R. R. *International Journal of Solids and Structures* **2006**, *43*, 2318.

(37)	Pawlak, A.; Galeski, A.; Rozanski, A. *Prog. Polym. Sci.* **2014**, *39*, 921.

(38)	Pawlak, A.; Galeski, A. *Macromolecules* **2005**, *38*, 9688.

(39)	Pawlak, A. *Polymer* **2007**, *48*, 1397.

(40)	Pawlak, A. *Colloid Polym. Sci.* **2013**, *291*, 773.

(41)	Fetters, L. J.; Lohse, D. J.; Richter, D.; Witten, T. A.; Zirkel, A. *Macromolecules* **1994**, *27*, 4639.

(42)	Fetters, L. J.; Lohse, D. J.; Milner, S. T.; Graessley, W. W. *Macromolecules* **1999**, *32*, 6847.

(43)	Schmidt-Rohr, K.; Spiess, H. W. *Macromolecules* **1991**, *24*, 5288.

(44)	Brown, E. N.; Willms, R. B.; Gray, G. T., III; Rae, P. J.; Cady, C. M.; Vecchio, K. S.; Flowers, J.; Martinez, M. Y. *Exp Mech* **2007**, *47*, 381.

Table of Contents Graphic